A Pulse Density Modulation Based Receiver Reactance Identification Method for Wireless Power Transfer System

Ruimin Dai, Ruikun Mai, *Senior Member, IEEE*, and Wei Zhou, *Member, IEEE*

***Abstract*—Tuning the receiver to match the resonant frequency with the working frequency plays an important role in improving the efficiency. One of the crucial steps in tuning is to determine the value or degree of detuning. In order to obtain the receiver reactance used to determine the detuning value, this article proposes a pulse density modulation (PDM)-based receiver reactance identification method. The parameter identification is performed as follows: implementing PDM technology on the active single-phase rectifier (ASPR) to bring in interharmonics and through Fast Fourier Transformation and least-square approximation, values of inductor and capacitor of the receiver can be identified. This estimation method only requires the magnitudes of voltage and current into ASPR for estimation. No extra hardware, no need to synchronize with the transmitter. In the experimental verification, four cases of resonant, inductive, and capacitive receivers are designed. Results show the maximum relative errors for estimation are within 5%, based on which the ASPR can tune the receiver as resonant. The situation that parameter deviates from the nominal value is also considered, even with deviations of mutual inductance and transmitter-side reactance, the estimation accuracy of receiver-side reactance is still at an average level.**

***Index Terms*—Inductive power transfer (IPT), parameter identification, receiver tuning, wireless power transfer (WPT).**

I. INTRODUCTION

Wireless power transfer (WPT) method has the advantages of electrical isolation and is environmentally friendly [1]. It is a promising charging method in various applications, such as electric vehicles, implanted medical devices, submarines, and so forth [2], [3]. Generally, the receiver must work with the resonant condition as shown in Fig. 1(a) to achieve maximum efficiency [4]. However, study [5] finds that, due to tolerance issue, aging, and variation in transmitter-receiver alignment, parameter values may deviate from the nominal values, causing the receiver to be nonresonant as shown in Fig. 1(b), where φ is no longer zero. Nonzero φ not only increases power dissipated in coils [6], but also prevents the system from achieving unity power factor [7]. The larger the φ, the lower the efficiency. So, monitoring φ is necessary for optimizing efficiency. But there are several challenges for acquiring φ: First, since the switching frequency of inductive power transfer (IPT) system can reach megahertz, the time slot is too short to use wireless communication for synchronizing the transmitter information to the receiver. Second, neither $\dot{U}_{oc}$ nor the receiver inductor can be directly measured during the charging process [8]. Currently, the existing methods to determine the receiver reactance can be roughly classified into three categories, which are briefly introduced below.

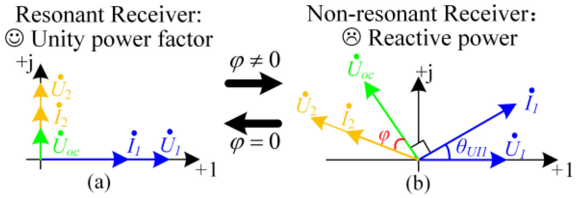

Fig. 1. Phasor diagrams of IPT system with (a) resonant receiver and (b) nonresonant receiver, where U_1/I_1 is the voltage/current output from inverter; U_2/I_2 is the voltage/current input into rectifier; Uoc, the induced voltage on receiver, is defined as $U_{\text{oc}} = j\omega M I_1$; φ is determined by receiver reactance and load.

1) Peak point tracking method. This method does not assess U_{oc} or receiver reactance, the basis is searching for the maximum/minimum point of a certain measurable parameter. Study in [9] proposes that the receiver will be resonant if the ratio of receiver current to transmitter current reaches the maximum. Literature [10] mentions that the ratio of power reflected from the receiver back to the transmitter is inversely proportional to receiver reactance. One limitation of this category is that the searching process for the peak point may be time-consuming and tracking accuracy may not be high. Another drawback is that the output power is varied during searching, while the IPT system is usually required to output stable rated power.
2) Additional measurement coil. Researches in [11] and [12] use a measurement coil to obtain U_{oc} to identify φ. The

Manuscript received December 5, 2021; revised March 1, 2022; accepted April 9, 2022. Date of publication April 13, 2022; date of current version May 23, 2022. This work was supported in part by the National Natural Science Foundation of China under Grant 51977184, in part by the Sichuan Youth Science and Technology Innovation Research Team under Grant 2020JDT0004, and in part by the Sichuan Science and Technology Program under Grant 2021YFH0039. Recommended for publication by Associate Editor A. Safaee. *(Corresponding author: Ruikun Mai.)*

The authors are with the Electrical Engineering Department, Southwest Jiaotong University, Sichuan 611756, China (e-mail: ruimindai1992@163.com; mairk@swjtu.edu.cn; wzhou@swjtu.edu.cn).

Color versions of one or more figures in this article are available at https://doi.org/10.1109/TPEL.2022.3167265.

Digital Object Identifier 10.1109/TPEL.2022.3167265

TABLE I
COMPARISON OF PAPERS ON RECEIVER REACTANCE IDENTIFICATION

Feature	Peak point Tracking [9] [10] [8]	Measurement Coil [11] [12]	Frequency Sweeping [13] [14]	This paper
Tx or Rx	Tx/Rx	Rx	Tx	Rx
No extra hardware	×/✓	×	✓	✓
Output unaffected	×	✓	×	✓
Fixed Frequency	✓	✓	×	✓

drawback is that in order to synchronize with the transmitter current, the measurement coil must be close enough to the transmitter, and the coil itself increases the overall size. Thus, this method is only suitable for situations with enough space.

3) Parameter identification. This article can also be classified into this category. This category assesses receiver reactance to obtain φ. Studies in [13] and [14] identify the receiver inductor and capacitor through sweeping the working frequency and analyzing the corresponding impedance on the transmitter. The limitation of frequency sweeping method is that, it is implemented in the transmitter-side and cannot provide stable power to the load if no other power regulator is used.

Based on the analysis above, two conclusions can be made: First, traditional receiver reactance identification methods always need extra hardware and synchronization of transmitter-side. Second, most previous parameter identification methods are based on transmitter-side and cannot provide stable output voltage during the identification without other power regulation. Therefore, this article proposes a pulse density modulation (PDM) based method to identify receiver reactance. An active single-phase rectifier (ASPR) is used to accomplish two tasks: First, applying PDM strategy to bring in interharmonics (interharmonic is the frequency which is not integer multiple of the fundamental frequency [15]) to help identify the receiver inductor and capacitor. Then, providing reactance to tune the receiver. The contributions of this article are as follows: 1) Neither wireless communication, synchronization with transmitter, nor extra hardware is needed. This feature greatly reduces the control complexity and overall size; 2) implemented on the receiver-side, output stable power during the identification process. This feature allows independent control of the receiver.

The features of papers above and this article are compared in Table I, where "Tx or Rx" means the identification is carried out from transmitter side (Tx) or receiver side (Rx).

To make this article self-contained, PDM technology is briefly introduced as follows. PDM strategy was first mentioned by Joung *et al.* [16], then, Fujita and Akagi [17] prove that PDM technology is an efficient control method because the zero-voltage-switching (ZVS) condition can be maintained during the power regulation. PDM has already been introduced into WPT system, for instance, Fan *et al.* [18] adopts the PDM strategy to control the semi-bridgeless active rectifier; furthermore, Fan *et al.* [19] also proposes an improved PDM strategy to reduce the output voltage ripple; Li *et al.* [20] puts forward a ZVS full-bridge converter to reduce the subharmonics, enlarge the modulation range, and speed up the response; besides, Li *et al.* [21] also proves that by substituting PDM-controlled converter for the conventional dc/dc converter used in maximum efficiency point tracking, the system can achieve ZVS with higher efficiency.

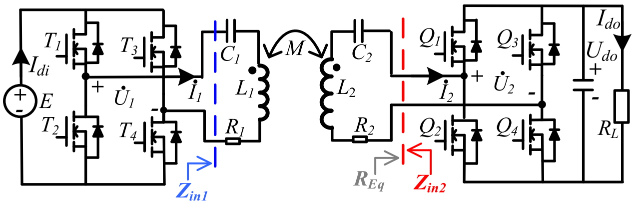

Fig. 2. SS-based IPT system with ASPR.

II. THEORETICAL ANALYSIS

A. Receiver-Side Reactance Analysis of SS Circuit

SS (series-compensated transmitter and series-compensated receiver) topology is one of the most widely used IPT circuits [22], [23]. A typical SS-based IPT system is shown in Fig. 2, the subscripts "1" and "2" are used to denote the transmitter side and receiver side parameters, respectively. L (C) represents the inductor (capacitor). E (I_{di}) is the dc input voltage (current). M is the mutual inductance, R_{L} is dc load. R_1 (R_2) is the equivalent series resistance (ESR) of transmitter (receiver) coil. U_{do} (I_{do}) represents the voltage (current) on dc load. The inverter and ASPR are composed of four MOSFETs (T1–T4 for inverter, Q1–Q4 for ASPR), respectively.

In this article, the real component provided by ASPR is viewed as R_{Eq}. The angular frequency is represented by ω, where $\omega = 2\pi f$, f is the operating frequency. Based on the Kirchhoff's Voltage Law, the SS topology shown in Fig. 2 can be described as (1), where $\dot{U}_1$ is the voltage vector out of inverter, which is referenced as zero phase degree. $\dot{I}_1 (\dot{I}_2)$ is the transmitter (receiver) current vector. Transferred efficiency, η, is one of the most important characteristics of the IPT system. With (1), η can be derived as (2), where $\overline{I_1}$ is the conjugate complex number of $\dot{I}_1$, $|\dot{I}_2|$ is the fundamental harmonic RMS value of $\dot{I}_2$, Re() represents the real component, P_{in} (P_{out}) represents the input power (output power on dc load), and X_2 denotes the reactance of the receiver coil: $X_2 = \omega L_2 - 1/(\omega C_2)$.

Based on (2), Fig. 3 illustrates the relationship between η and R_{Eq} under different X_2. It shows that despite the value of R_{Eq}, the larger the X_2, the smaller the η. Therefore, in order to maximize the efficiency, X_2 should be set to zero

$$\begin{cases} \dot{U}_1 = \left[R_1 + j(\omega L_1 - \frac{1}{\omega C_1})\right] \dot{I}_1 + j\omega M \dot{I}_2 \\ 0 = j\omega M \dot{I}_1 + \left[R_{Eq} + R_2 + j(\omega L_2 - \frac{1}{\omega C_2})\right] \dot{I}_2 \end{cases} \quad (1)$$

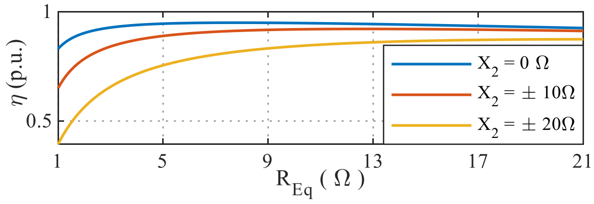

Fig. 3. Efficiency against load and receiver reactance, where $L_1 = 87.2$ uH, $L_2 = 70.61$ uH, $C_1 = 40.37$ nF, $M = 14.50$ uH, $R_1 = 0.2\ \Omega$, $R_2 = 0.2\ \Omega$.

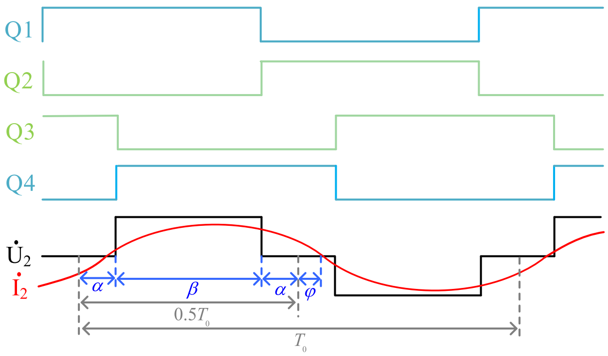

Fig. 4. Waveforms of the ASPR, the receiver is inductive.

$$\eta = \frac{P_{\text{out}}}{P_{\text{in}}} = \frac{\left|\dot{I}_2\right|^2 R_{Eq}}{\text{Re}(\dot{U}_1 \cdot \bar{I}_1)}$$
$$= \frac{(\omega M)^2 R_{Eq}}{(\omega M)^2 (R_2 + R_{Eq}) + R_1 \left[(R_2 + R_{Eq})^2 + X_2^2\right]}. \quad (2)$$

The receiver is resonant as X_2 equals zero, which means L_2 and C_2 should satisfy (3), where $\omega_0 = 2\pi f_0$ and f_0 is the receiver resonant frequency. But due to aging and misalignment, the values of L_2 and C_2 change and do not satisfy (3) anymore, resulting in nonzero X_2 and nonresonant receiver

$$\omega_0^2 L_2 C_2 = 1. \quad (3)$$

In order to adjust X_2, ASPR control strategy can be used. The operating principle of ASPR is illustrated in Fig. 4, where β is the pulse width, α is defined as $\alpha = 0.5(\pi\text{-}\beta)$, φ is the phase difference between $\dot{U}_2$ and $\dot{I}_2$, T_0 is the resonant period ($T_0 = 1/f_0$). If φ is positive (negative), $\dot{I}_2$ will lag behind (lead) the $\dot{U}_2$, and the ASPR is providing inductive (capacitive) reactance.

With Fourier expansion, U_2, the RMS value of fundamental harmonic in $\dot{U}_2$, can be derived as (4). Based on Fig. 4 and study in [11], I_{do} can be represented as (5), where I_2 is the RMS value of fundamental harmonic in $\dot{I}_2$. With (5), I_2 can be derived as (6). Notation X_{Eq}, the reactance provided by ASPR is represented as (7). With (4) and (6), R_{Eq} and X_{Eq} can be derived as (8). Consequently, if R_{Eq} and X_{Eq} are given, the corresponding β and φ can be calculated as (9)

$$U_2 = \frac{2\sqrt{2}}{\pi} U_{do} \sin\left(\frac{\beta}{2}\right) \cdot e^{j\varphi} \quad (4)$$

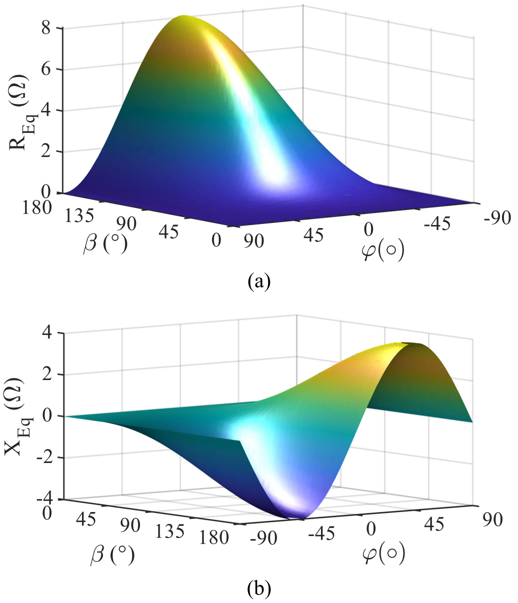

(a)

(b)

Fig. 5. Real component R_{Eq} and imaginary component X_{Eq} provided by ASPR, where $R_{\text{L}} = 10\ \Omega$. (a) R_{Eq} against φ and β. (b) X_{Eq} against φ and β.

$$I_{do} = \frac{1}{\pi} \int_{-\varphi+\frac{\pi}{2}-\frac{\beta}{2}}^{-\varphi+\frac{\pi}{2}+\frac{\beta}{2}} \sqrt{2} I_2 \sin(\omega t) d(\omega t)$$
$$= \frac{2\sqrt{2}}{\pi} I_2 \sin\left(\frac{\beta}{2}\right) \cos(\varphi) \quad (5)$$

$$I_2 = \frac{\pi I_{\text{do}}}{2\sqrt{2} \sin(\frac{\beta}{2}) \cos(\varphi)} \quad (6)$$

$$Z_{Eq} = U_2 / I_2 = R_{Eq} + jX_{Eq} \quad (7)$$

$$\begin{cases} R_{Eq} = \frac{4}{\pi^2} R_L \cos(\varphi)^2 (1 - \cos(\beta)) \\ X_{Eq} = \frac{4}{\pi^2} R_L \sin(\varphi) \cos(\varphi)(1 - \cos(\beta)) \end{cases} \quad (8)$$

$$\begin{cases} \varphi = \arctan \frac{X_{Eq}}{R_{Eq}} \\ \beta = \arccos\left(1 - \frac{\pi^2 X_{Eq}}{2R_L \sin(2\varphi)}\right) \end{cases}. \quad (9)$$

Based on (8), the resistive impedance and reactive impedance provided by ASPR can be illustrated in Fig. 5. The range of β (φ) is $[0, \pi]$ ($[-0.5\pi, 0.5\pi]$). The maximum R_{Eq} could be provided by ASPR is $8R_{\text{L}}/\pi^2$ with $\beta = \pi$ and $\varphi = 0$, and the maximum X_{Eq} is $\pm 4R_{\text{L}}/\pi^2$ with $\beta = \pi$ and $\varphi = \pm\pi/4$. If the required R_{Eq} or X_{Eq} exceeds $8R_{\text{L}}/\pi^2$ or $\pm 4R_{\text{L}}/\pi^2$, the ASPR method will not meet the requirements, other reactance compensation methods can be considered under this condition, such as capacitance matrix, variable inductor, etc.

B. *Identification of Receiver-Side Reactance*

To keep the receiver resonant, the relationship between X_2 and X_{Eq} must be as (10). To identify X_2, this section will analyze the underlying formula between the unknown set $\{L_2, C_2\}$ and other measurable circuit quantities

$$X_{Eq} = -X_2. \quad (10)$$

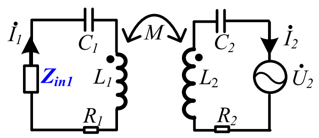

Fig. 6. Equivalent circuit when ASPR works with PDM.

The input impedance $Z_{\text{in}1}$ shown in Fig. 2 is defined as $Z_{\text{in}1} = \dot{U}_1/\dot{I}_1$. By solving (1), $Z_{\text{in}1}$ can be represented by (11). When the ASPR works with PDM strategy, from the perspective of receiver side, the topology can be described as in Fig. 6 and (12), where $\dot{U}_2$ is the voltage vector input to ASPR. Notation $Z_{\text{in}2}$ is defined as $Z_{\text{in}2} = \dot{U}_2/\dot{I}_2$. By solving (12), $Z_{\text{in}2}$ can be derived as (13)

$$Z_{\text{in1}} = \left[R_1 + j\left(\omega L_1 - \frac{1}{\omega C_1}\right)\right] + \frac{(\omega M)^2}{\left[R_{Eq} + R_2 + j(\omega L_2 - \frac{1}{\omega C_2})\right]} \tag{11}$$

$$\begin{cases} 0 = \left[Z_{\text{in1}} + R_1 + j(\omega L_1 - \frac{1}{\omega C_1})\right] \dot{I}_1 + j\omega M \dot{I}_2 \\ \dot{U}_2 = j\omega M \dot{I}_1 + \left[R_2 + j(\omega L_2 - \frac{1}{\omega C_2})\right] \dot{I}_2 \end{cases} \tag{12}$$

$$Z_{\text{in2}} = (R_2 + jX_2) + \frac{(\omega M)^2}{\left[2R_1 + 2j(\omega L_1 - \frac{1}{\omega C_1}) + \frac{(\omega M)^2}{R_{Eq}+R_2+jX_2}\right]}. \tag{13}$$

Based on (13), if ω changes to another value, a new set of $\{\omega, Z_{\text{in}2}\}$ can be obtained. One set of $\{\omega, Z_{\text{in}2}\}$ corresponds to one equation of (13). Assuming that values of R_1, R_2, L_1, C_1, and *M* are given, and R_{Eq} can be easily obtained on the receiver side, then, $\{L_2, C_2\}$ can be calculated from two equations of (13). This idea is the basic one for designing the process of parameter identification. Except SS topology, this principle is also applicable to other topologies, just by modifying the equation in (13) to the corresponding $Z_{\text{in}2}$ equation of the relevant circuit.

Based on (13), the magnitude of Z_{in2}: $|Z_{\text{in2}}|$, is shown as (14). At frequency ω, $|Z_{\text{in2}}|$ is specifically represented as $|Z_{\text{in2\_}\omega}|$. Equation (15) illustrates that $|Z_{\text{in2\_}\omega}|$ can be obtained from $|U_{2\_\omega}|$ and $|I_{2\_\omega}|$, where $|U_{2\_\omega}|$($|I_{2\_\omega}|$) is the amplitude of the $\dot{U}_2$ ($\dot{I}_2$) at frequency ω.

$$|Z_{\text{in2}}| = \left|\,(R_2 + jX_2) + \frac{(\omega M)^2}{\left[2R_1 + 2j(\omega L_1 - \frac{1}{\omega C_1}) + \frac{(\omega M)^2}{R_{Eq}+R_2+jX_2}\right]}\right| \tag{14}$$

$$|Z_{\text{in2\_}\omega}| = |U_{2\_\omega}|/|I_{2\_\omega}|. \tag{15}$$

Therefore, the process for identifying $\{L_2, \mathrm{C}_2\}$ can be derived as follows: First, obtaining at least two different sets of $\{\omega, |Z_{\text{in2\_}\omega}|\}$ based on (15). Second, using these sets of $\{\omega, |Z_{\text{in2\_}\omega}|\}$ to create multiple equations of (14) and derive $\{L_2, \mathrm{C}_2\}$ by solving (14).

It is very important to notice that, for mathematical equation which is error-free, the unknown set $\{L_2, \mathrm{C}_2\}$ solved by any two equations are identical. But in practical applications, because of the measurement errors and parameter tolerance, $\{L_2, \mathrm{C}_2\}$ derived from different equations will always be different. In order to find the most suitable $\{L_2, \mathrm{C}_2\}$ for all the $\{\omega, |Z_{\text{in2\_}\omega}|\}$ sets, the least-square approximation method is widely used [24], [25]. The basic principle of the least-square problem is to find the minimum residuals. Group L_2, C_2 into a vector of unknowns $X = (L_2, \mathrm{C}_2)^{\mathrm{T}}$. The residuals are defined as (16). *m* is the number of equations (14), y_{j} is the value of $|Z_{\text{in2\_}\omega}|$ at the *j*th set of $\{\omega, |Z_{\text{in2\_}\omega}|\}$, which can be obtained from (15). Notation $|Z_{\text{in2}}(j\omega, X)|$ is derived from (14) with $j\omega$ and *X*, where $j\omega$ is the value of ω in the *j*th set of $\{\omega, |Z_{\text{in2\_}\omega}|\}$ sets

$$r_j(X) = y_j - |Z_{\text{in2}}(j\omega, X)|,\ j = 1, 2, \ldots, m. \tag{16}$$

The estimated value of *X* can be obtained by solving the problem of (17), where *L* (*H*) is the lower (upper) bound for *X*

$$\min_{X\in[L,H]} f(X) = r_1^2(X) + r_2^2(X) + \cdots + r_m^2(X). \tag{17}$$

Based on (14), L_2 and C_2 are nonlinearly related to $|Z_{\text{in2\_}\omega}|$, thus, solving (17) is a nonlinear least-square problem. Generally, there are no direct equations for solving nonlinear least-square problem, iteration calculation is used for estimation under this condition [26].

C. Sequence Selection of PDM Strategy

Having built the estimation equations, the next step is to create multiple sets of $\{\omega, |Z_{\text{in2\_}\omega}|\}$ for identification. Proposal in [24] uses the fundamental and third-order harmonics of pulsewidth modulation strategy to perform this task; however, it is pointed out in [25] that only two frequency points may not be sufficient for accurate estimation. And it is preferred to output stable rated voltage during the identification process [27]. So, the PDM strategy, having multiple interharmonics, will be adopted to achieve the goals of estimation and stable output. Since the small magnitudes usually have relatively high sensitivity to measurement errors, this part will design interharmonics of PDM strategy with larger amplitudes, which is the same as the PDM design of Section II-C in [28].

Working frequencies for both inverter and ASPR are f_0. The ASPR modulates $\dot{U}_2$ using the pulses synchronized with the $\dot{I}_2$. The operating principle of PDM is represented in Fig. 7, where T_0 is the resonant period of the system ($T_0 = 1/f_0$), and $0.5T_0$ is half of the resonant cycle. The smallest time of one mode is $0.5T_0$. The PDM technique works by connecting the circuit to the inverter during $p0.5T_0$ (power mode) and then short-circuiting the circuit during $n0.5T_0$ (short mode). The time of one PDM full cycle is $0.5(p+n)T_0$. The pulse density of PDM is defined as $p/(p+n)$

$$R_{Eq} = \frac{8R_L}{\pi^2}\left(\frac{p}{p+n}\right)^2 = \frac{8R_L}{\pi^2}\text{density}^2. \tag{18}$$

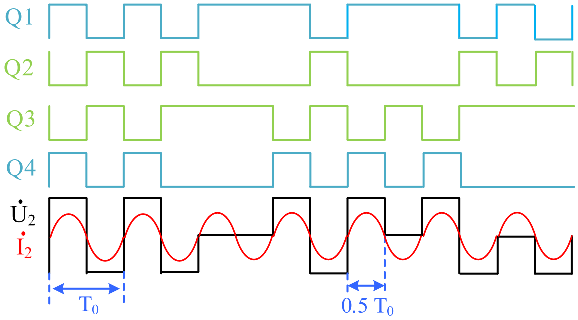

Fig. 7. PDM technique operating principle.

TABLE II
NUMBER AND POSITION OF FREQUENCY POINTS IN PDM INTERHARMONICS

	Number of frequency points: Position of the frequency points
p=2	2: $f_0/2$, $3f_0/2$
p=3	4: $f_0/3$, $2f_0/3$, $4f_0/3$, $5f_0/3$
p=4	6: $f_0/4$, $2f_0/4$, $3f_0/4$, $5f_0/4$, $6f_0/4$, $7f_0/4$
p=5	8: $f_0/5$, $2f_0/5$, $3f_0/5$, $4f_0/5$, $6f_0/5$, $7f_0/5$, $8f_0/5$, $9f_0/5$

Based on [29], R_{Eq} can be derived as (18). To keep constant output voltage, the pulse density [denoted as "density" in (18)] should be fixed. This is the main reason why the popular delta–sigma-based PDM strategy is not suitable here because the delta–sigma strategy is used to adjust the output voltage [30], while in this article which focuses on receiver-reactance estimation, the output voltage is fixed at the rated value. As mentioned in [19], the more evenly the power mode distribution, the smaller the ripple of the output voltage, so, this article sets pulse density as 0.5, which means $p = n$ and helps evenly distribution. The smallest value of p is 2.

The relationship between the locations of the frequency points and p is represented as (19), the points equal to or larger than $2f_0$ are ignored because their magnitudes are usually relatively small and require a higher sampling rate. Based on (19), p and corresponding frequency points can be concluded in Table II. Notice that some of these points will be filtered later, because several points are repeated, for example, $2f_0/4$ equals $f_0/2$, and points that are likely to be interfered by adjacent points should be deleted

$$f_j = \left(1 \pm \frac{j}{p}\right) f_0,\ j = 1, 2, \ldots, p-1. \tag{19}$$

As aforementioned, it is necessary to create multiple frequency points for parameter identification, and signals with larger amplitudes are preferred for data collection. Therefore, the rule for selecting PDM sequences can be derived as follows: first, bringing in multiple frequency points. To perform this task, this article sets p to sweep from 2 to 5. Then, for each p, design more than one waveform (different waveforms are named as sequence x, the number of the digit of x is p+n, the value of the digit of x is 1/0, where 1/0 represents power/short mode). The basis for this step is that waveforms with the same p have the same set of frequency positions as shown in Table II, while at the same frequency position, different sequences are likely to have different amplitudes [Fast Fourier Transformation (FFT) method will be used in this step to derive the amplitudes]. Consequently, at each point, the sequence with the maximum amplitude will be selected.

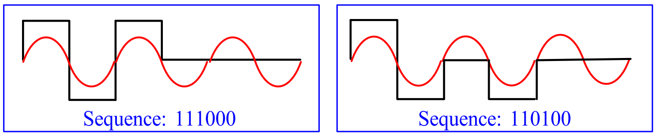

(a) (b)

Fig. 8. Different sequences for $p = 3$, where black (red) wave is U_2 (I_2).

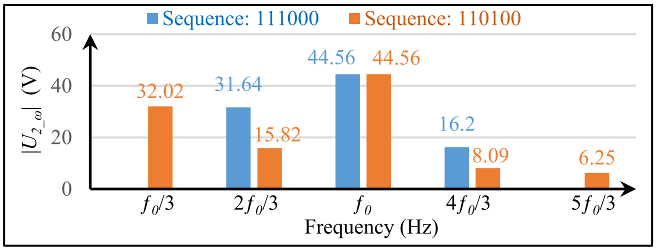

Fig. 9. Frequency spectrum for $p = 3$, where $E = 70$ V.

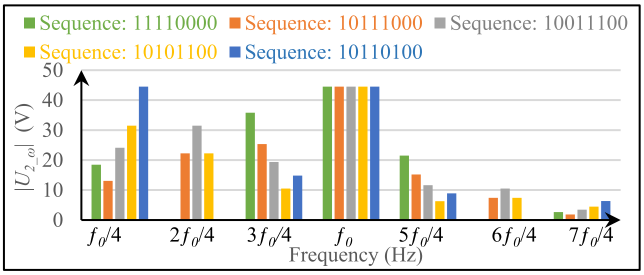

Fig. 10. Frequency spectrum for $p = 4$, where $E = 70$ V.

For $p = 2$, only one sequence exists: 1100, thus, this sequence will be directly adopted. For $p = 3$, at least two sequences exist as illustrated in Fig. 8: 111000 and 110100. Next, FFT method is used to illustrate the frequency spectrums as shown in Fig. 9.

Based on Fig. 9, for 111000, $|U_{2\_\omega}|$ for $f_0/3$ and $5f_0/3$ are zero, while the amplitudes for $2f_0/3$, $4f_0/3$ are larger than that of 110100. The sequence should be selected to maximize magnitudes, therefore, for $p = 3$, amplitudes of $|U_{2\_\omega}|$ and $|I_{2\_\omega}|$ at $f_0/3$, $5f_0/3$ ($2f_0/3$, $4f_0/3$) are collected when the sequence is 110100 (111000).

For $p = 4$, 5, at least five sequences exist, their frequency spectrums are shown in Figs. 10, and 11, respectively. In Fig. 11, $9f_0/5$ is not shown because $|U_{2\_\omega}|$ at $9f_0/5$ is too small, which is 2.9, while $|U_{2\_\omega}|$ at $2f_0/5$ is 34.26 (2.9 is an order of magnitude smaller than 34.26). And this point requires a higher sampling rate, so, it is not used in this article.

For help select, two criteria are adopted: the first criterion is to start from a small p value. Because based on Table II, smaller p involves less interharmonics. The smaller the number of interharmonics, the larger the gap between interharmonics, and the less interference to spectrum analysis. Thus, $f_0/2$ and

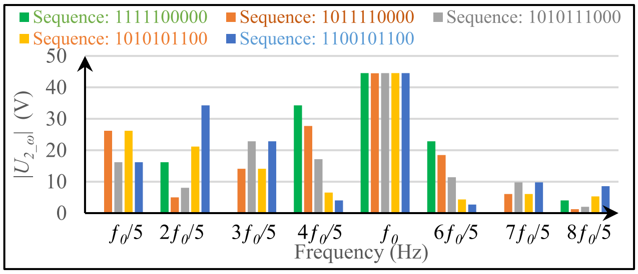

Fig. 11. Frequency spectrum for $p = 5$, where $E = 70$ V.

TABLE III
PROPER SEQUENCES FOR CREATING INTERHARMONICS

Seq No.	Sequence	Frequency Point
1	1100	$f_0/2$, f_0, $3f_0/2$
2	110100	$f_0/3$, $5f_0/3$
3	111000	$2f_0/3$, $4f_0/3$
4	10110100	$f_0/4$, $7f_0/4$
5	1011110000	$f_0/5$
6	1100101100	$2f_0/5$, $3f_0/5$, $7f_0/5$, $8f_0/5$

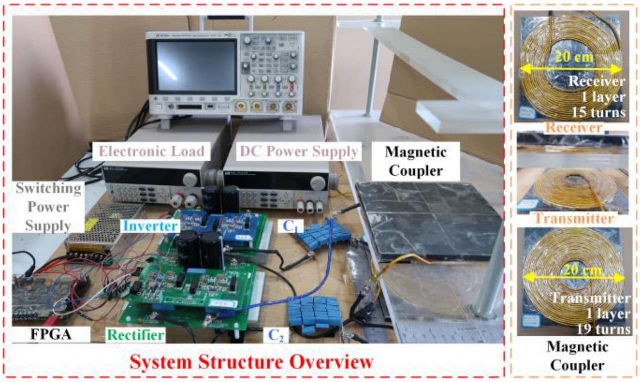

Fig. 12. Photo of the prototype.

TABLE IV
CASES FOR IDENTIFICAION

Case	R_L (R_{Eq}) (Ω)	C_2 (Deviation) (nF)	X_2 (Ω)	Gap (cm)	M (uH)	L_1 (uH)	L_2 (uH)	C_1 (nF)	R_1 / R_2 (Ω)
1	38 (7.70)	50.61 (0.64%)	0.24	9.50	14.50	85.71	69.72	40.94	0.2
2		53.30 (5.99%)	2.11						
3	15 (3.04)								
4		44.90 (10.72%)	-4.47						

$3f_0/2$ for $p = 2$ are adopted while $2f_0/4$ and $6f_0/4$ for $p = 4$ are not used. The second criterion is that, according to [31], the larger/smaller the adjacent interharmonics, the more/less the interference for identifying the other interharmonics. That means two standards for selecting, the first standard is that the closer to f_0 (based on Figs. 10 and 11, amplitudes at f_0 are the largest), the greater the interference to FFT analysis. So, $3f_0/4$, $5f_0/4$ for $p = 4$ in Fig. 10, and $4f_0/5$, $6f_0/5$ for $p = 5$ in Fig. 11 are not used. At this stage, the remaining points on Figs. 10 and 11 are $f_0/4$, $7f_0/4$, $f_0/5$, $2f_0/5$, $3f_0/5$, $7f_0/5$, and $8f_0/5$. For further selection, the second standard is used: for points where more than one sequences have the maximum magnitudes, choose the sequence that has a smaller magnitude in the adjacent point. For instance, for $f_0/5$ in Fig. 11, both 1011110000 (orange) and 1010101100 (yellow) have the maximum magnitude, but at the adjacent point: $2f_0/5$, the former one has smaller magnitude, so, 1011110000 is selected for $f_0/5$. Furthermore, for $3f_0/5$ and $7f_0/5$ in Fig. 11, both 1100101100 (blue) and 1010111000 (gray) have the maximum magnitudes. The problem is that at their adjacent points: $2f_0/5$ and $8f_0/5$, the blue one is larger than the gray, while at the other adjacent points: $4f_0/5$ and $6f_0/5$, the gray one is larger than blue. Under this situation, control strategy is considered. Since1100101100 (blue) has already been adopted for points $2f_0/5$ and $8f_0/5$, this sequence is also used for $3f_0/5$ and $7f_0/5$.

Consequently, Table III concludes the sequences and frequency points used for building parameter identification model. By sweeping the sequence from Seq 1 to Seq 6, there are 14 frequency points. In some cases, these 14 points may not be fully usable. For instance, due to the parameter settings, at some point, $|I_{2\_\omega}|$ is too small to be measured, causing that point cannot be used (this situation can be observed in Case 4 of Fig. 15). And since L_2 and C_2 are not given, it is almost impossible to predetermine which point will have unusable $|I_{2\cdot\omega}|$. To solve these problems, if the usable points in Table III cannot derive a good estimation, one needs to increase the value of p to bring in more interharmonics and use the new points together with the usable points in Table III for identification.

III. EXPERIMENTAL VERIFICATION

As shown in Fig. 12, an experimental prototype of SS-compensated IPT system is built. This experiment is just for theoretical validation. For different applications in real practice, the size and power capacity can be scaled down/up accordingly.

A. *Experimental Setup*

The full-bridge inverter and ASPR are composed of four MOSFETs (CREE C2M0080120D), respectively. The switching signals of MOSFETS are provided by an FPGA (ALINX AX7020). The switching power supply is used to power the driver board of the inverter. The inductors are wound with Litz wire (0.1∗400, 2.85 mm width). Receiver pad is centered on top of the transmitter pad. Ferrite (1 cm thickness) is inserted for enhancing and guiding the flux, and it is assumed that the ferrite does not saturate under normal operation. LCR meter (Agilent E4980A) is applied to measure the values of inductance, capacitance, and ESR. The waveforms are analyzed and recorded by the oscilloscope (Keysight infiniiVision DSOX3014T). The dc power supply (ITECH IT6942A 60V/15A/360W) and electronic load (ITECH IT8812C 120V/60A/250W) are applied as E and R_{L} to run the system.

The coupling coefficient in the experiment, 0.18 (derived from Table IV), is not strong enough to cause the current distortion [32]. So, the ASPR will just use the pulse synchronized with $\dot{I}_2$ [29]. Additionally, study [33] mentions that current discontinuity may happen under light load conditions. Since this problem is

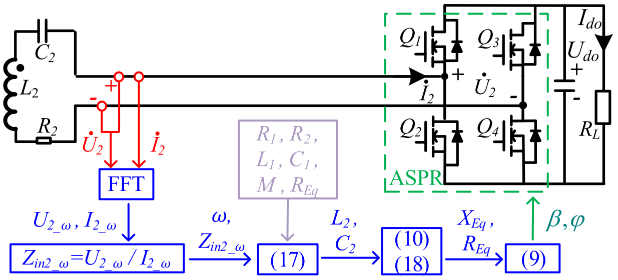

Fig. 13. Control strategy and flowchart.

TABLE V
PARAMTERS FOR LEAST-SQUARE APPROXIMATION

Parameter	Lower bound	Upper bound	Parameter	Lower bound	Upper bound
L_2	60 uH	90 uH	C_2	30 nF	70 nF

TABLE VI
SAMPLE RATE

Seq No.	1	2	3	4	5	6
Maximum Signal Frequency (kHz)	127.50	141.67	141.67	148.75	136	136
Sample Frequency (MHz)	1.28	1.42	1.42	1.49	1.36	1.36

independent of the proposal in this article, it will not be further discussed.

The inverter outputs normal rectangular waveforms with f_0. The experiment process is as follows: first, according to Table III, sweeping $\dot{U}_2$ from Seq 1 to Seq 6, collecting $\dot{U}_2$ and $\dot{I}_2$ at these six sequences; then, using the control strategy illustrated in Fig. 13 for identification and tuning.

B. Parameter Identification

Just for theoretical verification, f_0 is set as 85 kHz, and the power on dc load is 145 W. Four cases are designed in Table IV, where "Deviation" after "C_2" represents the deviation percentage from the resonant capacitance [which is 50.29 nF according to the L_2 and (3)]. In the receiver reactance identification, L_2 and C_2 will be identified as other parameters given in Table IV. The bounds for the least-square approximation are shown in Table V, which are set between 0.6and 1.4 multiples of the nominal values just by experience. Bounds may have some influences on the estimation results, but these problems are about the least-square approximation itself, so, this article will not further investigate it. Based on the Nyquist criterion, the sample rate must be at least twice the maximum signal frequency. This article sets the sample rate to 10 times the maximum signal frequency. Thus, based on Table III, the sample frequencies can be designed as in Table VI.

To achieve the sample rate in Table VI, many hardware can be used, for instance, the combination of current sensor MCX 1101 (1.5 MHz bandwidth) and analog-to-digital converter AD7760 (2.5MSPS sampling rate, 24 bit). This experiment is only for demonstrating the theory, thus, for simplicity, the data are collected through oscilloscope, and then extracted to computer, and MATLAB is used for analysis.

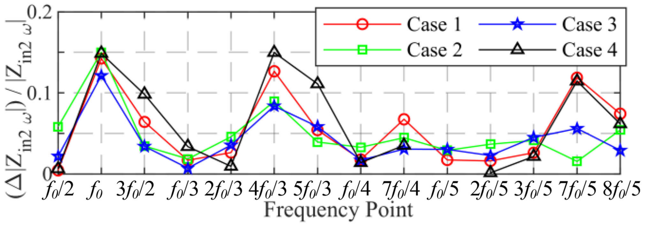

Fig. 14. Relative error of measured impedance at each frequency point.

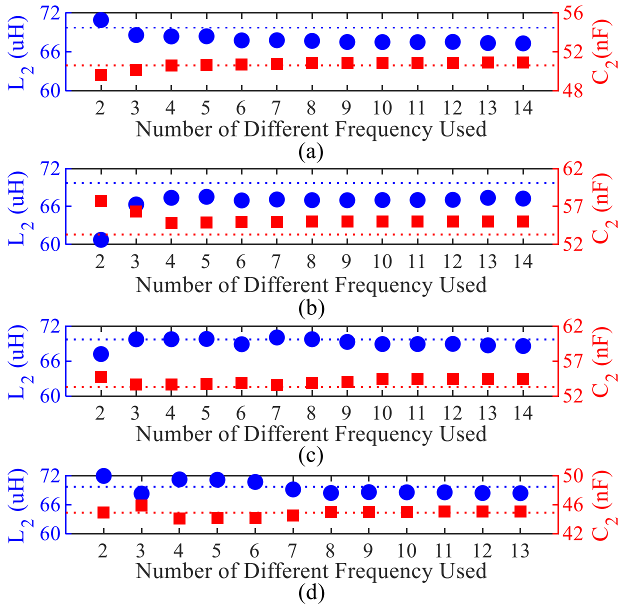

Fig. 15. Identified L_2 (blue dot) and C_2 (red square). The dotted line represents the nominal value. (a) Case 1. (b) Case 2. (c) Case 3. (d) Case 4.

TABLE VII
CORRESPONDING FREQUENCY POINTS FOR ESTIMATION

Number of Frequency used	Corresponding Frequency Point
2	$f_0/2$, f_0
3	Points above + $3f_0/2$
4	Points above + $f_0/3$
5	Points above + $2f_0/3$
6	Points above + $4f_0/3$
7	Points above + $5f_0/3$
8	Points above + $f_0/4$
9	Points above + $7f_0/4$
10	Points above + $f_0/5$
11	Points above + $2f_0/5$
12	Points above + $3f_0/5$
13	Points above + $7f_0/5$
14	Points above + $8f_0/5$

Fig. 14 shows the measurement errors for each frequency. Fig. 15 illustrates the identification results, where the dotted line represents the nominal value. The horizontal axis of Fig. 15 is explained in Table VII. The estimated values at the last points of Fig. 15 are shown in Table VIII.

TABLE VIII
IDENTIFIED RESULTS

	Case 1	Case 2	Case 3	Case 4
L_2 (uH) **(Relative error)**	67.27 (3.51%)	67.23 (3.53%)	68.59 (1.62%)	68.40 (1.89%)
C_2 (nF) **(Relative error)**	50.89 (0.55%)	55.02 (3.25%)	54.47 (2.20%)	45.09 (0.42%)

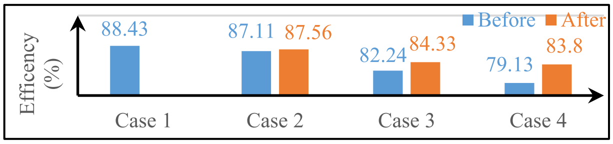

Fig. 16. Efficiencies before and after tuning, output power keeps at 145 W.

Based on Fig. 14, the measurement errors are below 16%. Because of the measurement error, as shown in Fig. 15, the estimation errors are large when there are only two frequencies, but as the number of frequencies increases, the accuracy improves. This phenomenon proves that by increasing the frequency number, the problem of measurement errors can be overcome to some degree.

In Fig. 15, for Case 1–Case 3, all the 14 points are used. For Case 4, current at $f_0/5$ is too small, thus, this point is not collected. The initial value for number of frequencies used is 2 because there are two unknowns to be identified. As the number of frequencies used increases, the estimated results have some fluctuations. This phenomenon is common in iteration calculation, which can also be observed in [25]. Although the fluctuation exists, the least-square method enables the estimated results to converge toward the reference value as the number of frequency points increases. Based on Table VIII, the relative errors are below 5%, which proves that regardless of receiver reactance, this method can obtain a reasonably accurate estimation. The computer used to do the iteration task in this study is ThinkPad T450S (Intel Core i5-5200U @2.2 GHz, 8 GB RAM), it takes from 2 to 5 s to obtain the estimated L_2 and C_2 for one case.

C. Efficiencies and Captured Waveforms

After obtaining L_2 and C_2, the next step is to tune the receiver if the receiver is out of resonant. The efficiencies before and after tuning are concluded in Fig. 16. For a fair comparison, before and after the tuning, R_{Eq} and output power on dc load are the same. For Case 1, the receiver is approximately resonant, so this case is not tuned. The captured waveforms before and after tuning for Case 2–Case 4 are shown in Figs. 17–19, respectively. System loss breakdown is shown in Fig. 20, studies in [34], [35], and practical measurements are used to calculate these losses.

Based on Fig. 16, for Case 2, Case 3, and Case 4, efficiency increases are 0.45%, 2.09%, and 4.67%, respectively. Although Case 2 and Case 3 have the same X_2, the later one has a larger efficiency improvement, proving that the smaller the R_{Eq}, the greater the impact of X_2 on efficiency reduction. In addition, by comparing Case 3 and Case 4, it can be concluded that the more detuned, the more the efficiency improvement after tuning.

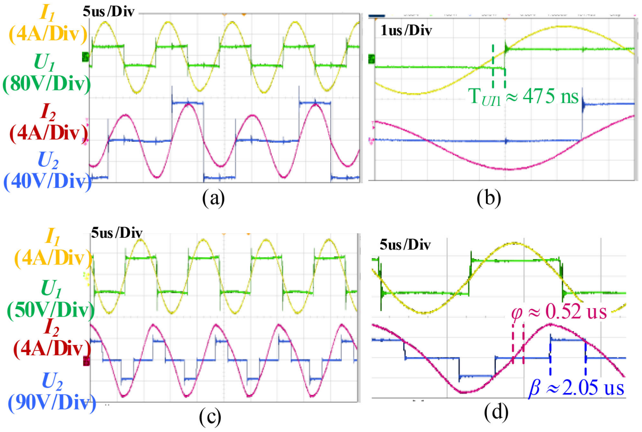

(a) (b)
(c) (d)

Fig. 17. Captured waveforms for Case 2, output power keeps around 145 W. (a) Waveforms before tuning. (b) Zoom-in waveforms before tuning. (c) Waveforms after tuning. (d) Zoom-in waveforms after tuning.

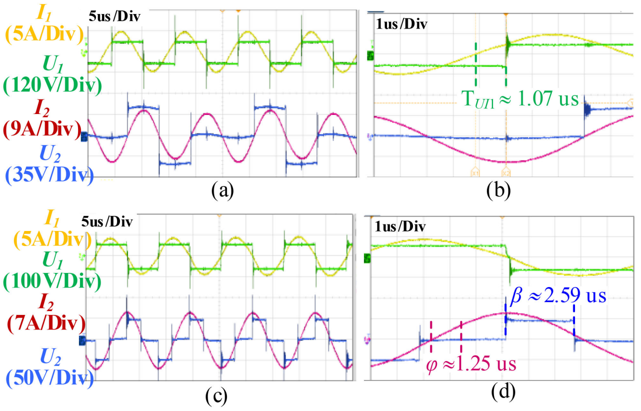

(a) (b)
(c) (d)

Fig. 18. Captured waveforms of Case 3, output power keeps around 145 W. (a) Waveforms before tuning. (b) Zoom-in waveforms before tuning. (c) Waveforms after tuning. (d) Zoom-in waveforms after tuning.

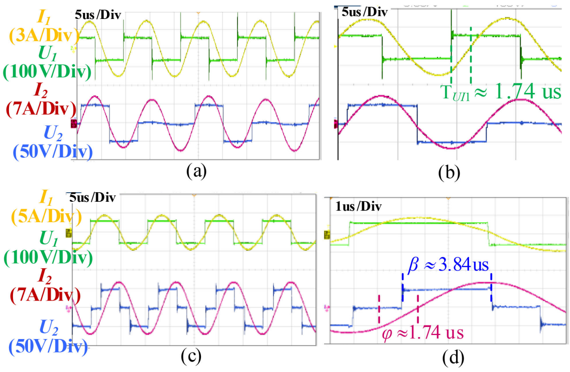

(a) (b)
(c) (d)

Fig. 19. Captured waveforms of Case 4, output power keeps around 145 W. (a) Waveforms before tuning. (b) Zoom-in waveforms before tuning. (c) Waveforms after tuning. (d) Zoom-in waveforms after tuning.

There are two main functions of Figs. 17–19: 1) The pictures before tuning represent the receiver is detuned, which proves the parameter settings in Table IV. 2) The pictures after tuning represent the system is resonant, which demonstrates the accuracy of the proposed parameter identification method and the correctness of ASPR adjusting equations as (9). To help

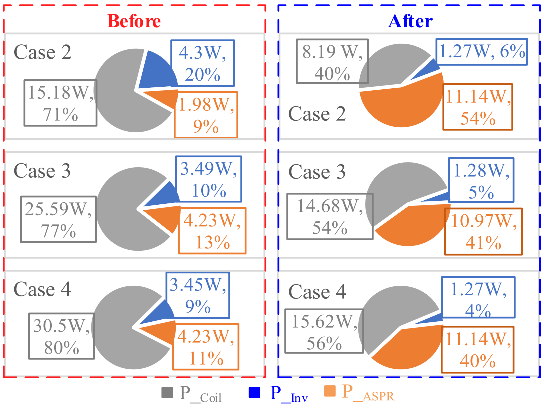

Fig. 20. Power loss distribution for the three cases, where $P\_{\rm Inv}$ (blue), $P\_{\rm ASPR}$ (orange), and $P\_{\rm Coil}$ (gray) represent power loss in the inverter, ASPR, and coil, respectively. The output power keeps around 145 W.

understand, take Case 2 as an example (Case 3 and Case 4 can also be studied as the Case 2 analysis). Based on (1), (20) is derived, where $X_{\rm i} = \omega L_{\rm i} - 1/(\omega C_{\rm i})$, $i = 1, 2$. Symbols T_{UI1} and θ_{UI1} [shown in Fig. 1(b)] represent the time difference and phase difference between U_1 and I_1, respectively

$$\begin{cases} T_{UI1} = \frac{\theta_{UI1}}{2\pi}T_0 \\ \theta_{UI1} = a\tan\left\{\frac{[X_2^2+(R_{Eq}+R_2)^2]X_1-X_2M^2\omega^2}{[X_2^2+(R_{Eq}+R_2)^2]R_1+(R_{Eq}+R_2)M^2\omega^2}\right\} \end{cases}. \tag{20}$$

Before the tuning, according to (20) and Case 2 setting in Table IV, T_{UI1} is 475 ns and the receiver is inductive; Based on the captured waveforms in Fig. 17(b), U_1 lags I_1 for approximately 475 ns, which is in accordance with the calculated value. Then, after tuning, according to (20) and Case 2 estimations in Table VIII, φ and β are derived as 0.52 and 2.05 us, respectively, which can also be observed in Fig. 17(d). Based on Fig. 17(c) and (d), U_1 and I_1 are almost in phase (I_1 slightly lags behind U_1 to achieve ZVS), which proves that with the identified results the receiver could achieve resonance.

Fig. 20 illustrates where the energy goes before and after tuning: before tuning, energy is mainly lost in the coil, this is because the nonzero receiver reactance increases the energy stored and released in the coils, which increases the coil losses [7]; and the hard switching increases the inverter loss. After tuning, the loss caused by ASPR increases. This is because the phase-shift strategy is used by the ASPR to adjust the resistance and reactance, which causes hard-switching, this problem is not the focus of the article and will not be discussed.

Efficiency improvement under load variation is illustrated in Fig. 21. It proves that the larger the X_2, the greater the efficiency improvement brought by tuning resonance. In addition, the smaller the R_{Eq}, the greater the efficiency decreasing brought by detuning. These appearances are in accordance with the theoretical analysis of Fig. 3.

D. Outputs During Sequence Sweeping

Fig. 22 represents the voltages and currents for Case 1. The *Udo* and *Ido* are almost fixed as the sequence changes, proving that the proposal can achieve constant outputs during the identifying process. Sequence has an influence on *I2*, the fluctuation of *I2* is caused by the number of rising and falling processes, which is analyzed in [33].

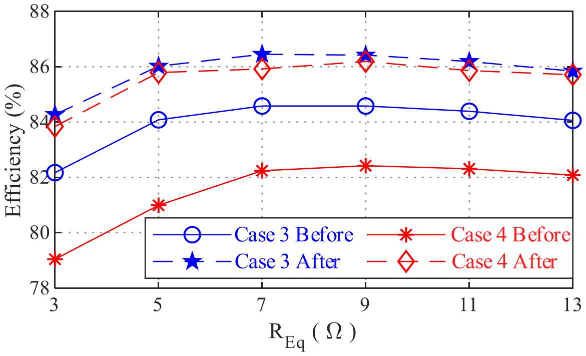

Fig. 21. Efficiencies before tuning and after tuning during load variation, where $P_{\rm out}$ keeps around 145 W, $R_{\rm L} = 18\ \Omega$, other parameters are the same as Table IV.

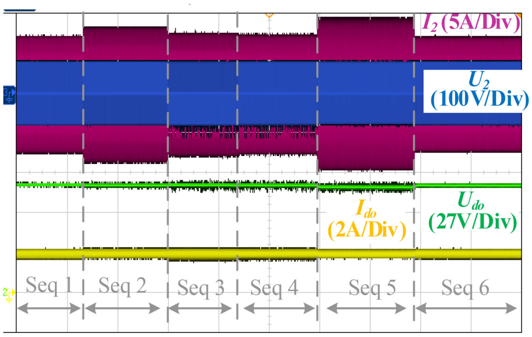

Fig. 22. Captured waveforms of voltages and currents for Case 1.

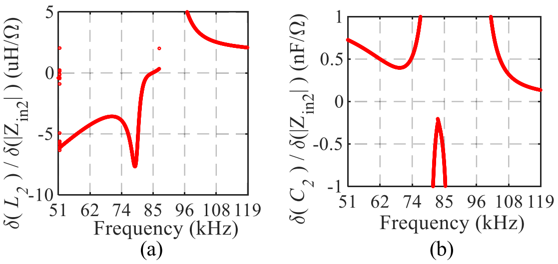

(a) (b)

Fig. 23. Influence analysis of impedance on (a) L_2, (b) C_2, for Case 1.

E. Influence of Measurement Error

In the experiment, voltage and current are used to obtain receiver reactance. Equivalently, the measured parameters can be regarded as one variable: $|Z_{\rm in2}|$. Taking Case 1 as an example, based on (13), the rates of change of L_2 and C_2 with respect to $|Z_{\rm in2}|$ are represented in Fig. 23, where $\delta(L_2)/\delta(|Z_{\rm in2}|)$ and $\delta(C_2)/\delta(|Z_{\rm in2}|)$ represent the partial derivative of L_2 and C_2 with respect to $|Z_{\rm in2}|$, respectively. Sensitivity in region $< f_0$ is higher than that of region $> f_0$, and L_2 is more sensitive than C_2 to measurement errors.

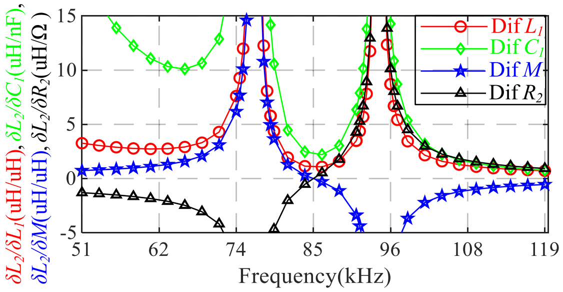

Fig. 24. Influence analysis of parameter deviations on L_2, Case 1.

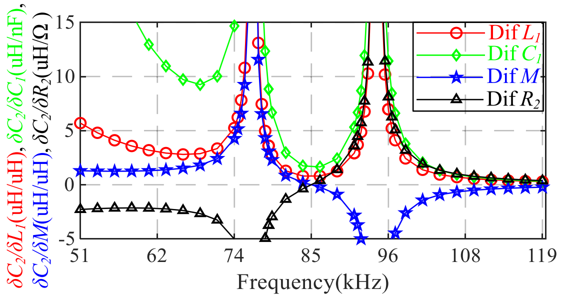

Fig. 25. Influence analysis of parameter deviations on C_2, Case 1.

F. Influence of Parameter Deviation

In the above experiment, except L_2 and C_2, all the other parameters of (13) are assumed to be the given nominal values. But in actual applications, due to the parameter tolerance, aging, misalignment, temperature, etc., the actual values of circuit parameters may deviate from the nominal values. Therefore, this part will study the influence of parameter deviations. Based on (13), there are total five parameters (R_1, R_2, L_1, C_1, and M) to be considered in the influence of estimating L_2 and C_2. To help analysis, taking the partial derivative of L_2 and C_2 with respect to these parameters individually, the rate of change of L_2 and C_2 with respect to R_1 is shown in (21), which equals zero, meaning that the estimation is not affected by R_1; to R_2 is shown in (22), where the notations A, B, C, and D are defined in (23); to M is shown in (24); to L_1 is shown in (25); to C_1 is shown in (26). With these equations, taking Case 1 as an example, the influences can be illustrated in Figs. 24 and 25

$$\frac{\partial L_2}{\partial R_1} = 0, \frac{\partial C_2}{\partial R_1} = 0 \tag{21}$$

$$\frac{\partial L_2}{\partial R_2} = \frac{A}{\omega D}, \frac{\partial C_2}{\partial R_2} = \frac{\partial L_2}{\partial R_2}\frac{1}{C} \tag{22}$$

$$\begin{cases} A = 2(R_2X_1 + R_{Eq}X_1 - R_2Z_{\text{in1\_Im}} - R_{Eq}Z_{\text{in1\_Im}}) \\ B = X_1 - Z_{\text{in1\_Im}}, C = (\frac{D-\omega^2M^2}{2B} + \omega L_2)^2 \\ D = \sqrt{(\omega^2M^2)^2 - A^2} \\ Z_{\text{in1\_Im}} = X_1 - \frac{\omega^2M^2X_2}{(R_2+R_{Eq})^2+X_2^2} \end{cases} \tag{23}$$

$$\frac{\partial L_2}{\partial M} = \frac{\omega M(D-\omega^2M^2)}{BD}, \frac{\partial C_2}{\partial M} = \frac{\partial L_2}{\partial M}\frac{1}{C} \tag{24}$$

TABLE IX
ESTIMATIONS WITH M UNGIVEN

	Case 1	**Case 2**	**Case 3**	**Case 4**
L_2 (uH) **(Relative error)**	68.89 (1.19%)	68.52 (1.72%)	70.33 (0.87%)	69.46 (0.37%)
C_2 (nF) **(Relative error)**	50.75 (0.28%)	54.92 (3.04%)	54.33 (1.93%)	44.94 (0.9%)
M (uH) **(Relative error)**	18.77 (29.45%)	17.71 (22.14%)	18.65 (28.62%)	18.85 (30%)

TABLE X
ESTIMATIONS WITH L_1 AND C_1 UNGIVEN

	Case 1	**Case 2**	**Case 3**	**Case 4**
L_2 (uH) **(Relative error)**	67.99 (2.48%)	67.68 (2.93%)	69.61 (0.16%)	68.30 (2.04%)
C_2 (nF) **(Relative error)**	50.84 (0.45%)	55 (3.19%)	54.42 (2.10%)	45.07 (0.38%)
L_1 (uH) (Relative error)	80 (66.62%)			
C_1 (nF) **(Relative error)**	35.79 (12.58%)	41 (0.15%)	35 (14.51%)	37.44 (8.55%)

TABLE XI
ESTIMATIONS WITH M, L_1, AND C_1 UNGIVEN

	Case 1	**Case 2**	**Case 3**	**Case 4**
L_2 (uH) **(Relative error)**	65.01 (6.76%)	65.12 (6.60%)	66.52 (4.59%)	65.33 (6.30%)
C_2 (nF) **(Relative error)**	51.08 (0.93%)	55.26 (3.68%)	54.70 (2.63%)	45.33 (0.96%)
L_1 (uH) (Relative error)	80 (66.62%)			
C_1 (nF) (Relative error)	35 (14.51%)			
M (uH) (Relative error)	20 (37.86%)			

$$\frac{\partial L_2}{\partial L_1} = \frac{D-\omega^2M^2}{2B^2} + \frac{(R_2+R_{Eq})A}{BD}, \frac{\partial C_2}{\partial L_1} = \frac{\partial L_2}{\partial L_1}\frac{1}{C} \tag{25}$$

$$\begin{aligned} \frac{\partial L_2}{\partial C_1} &= \left(\frac{D-\omega^2M^2}{2B^2} + \frac{(R_2+R_{Eq})A}{BD}\right)\frac{1}{\omega^2C_1^2}, \\ \frac{\partial C_2}{\partial C_1} &= \frac{\partial L_2}{\partial C_1}\frac{1}{C}. \end{aligned} \tag{26}$$

Based on Figs. 24 and 25, the surge of sensitivities appears in the vicinity of [74, 79 kHz] and [90, 96 kHz]. The high sensitivity region is located around the system resonant frequency, so, it is better to not use the frequency points adjacent to the resonant frequency to avoid this region. Notice that high sensitivity does not necessarily mean poor estimation result, which is influenced by many factors. Furthermore, M is the factor most likely to deviate from the nominal value in practical applications, leading to relative error in the estimation. Taking the derivative equal to 2 as an example, in this experiment, 10% of M deviation will cause 4.2% relative error of L_2 (14.5*0.1*2/69.72 = 4.2%).

Next, identifying L_2 and C_2 will be carried out again as three situations are considered: 1) The nominal value of M is unusable; 2) the nominal values of L_1 and C_1 are unusable; and 3) the nominal values of M, L_1, and C_1 are unusable. The data of $\{\omega, |Z_{\text{in2\_}\omega}|\}$ collected in Section III-B is used for estimation. The results are shown in Tables IX–XI, respectively, where the

TABLE XII
PARAMTERS FOR LEAST-SQUARE APPROXIMATION

Parameter	L_1 **(uH)**	C_1 **(nF)**	L_2 **(uH)**	C_2 **(nF)**	M **(uH)**
Bounds	[80, 90]	[35, 45]	[60, 90]	[30, 70]	[10, 20]

TABLE XIII
COMPARISON OF THIS ARTICLE AND RELATIVE PAPERS

	Estimated Parameter	**Estimation Algorithm (Estimation Speed)**	**Maximum Relative Error**
[36]	R_{Eq}	4^{th}-order differential approximation (Fast)	> 7%
This paper	L_1, L_2, M, C_1, C_2	Least-square approximation (Relative fast)	6.76% for L_2, 3.68% for C_2
[37]	M, R_{Eq}	Equation calculation (Fast)	6.68% for M, 5.60% for R_{eq}
[27]		Ferrari Method (Fast)	5.70% for M, 5.50% for R_{eq}
[13]	M, R_{Eq}, C_2, L_2	Adaptive differential evolution (Slow)	< 5% for L_2, C_2
This paper	L_2, C_2	Least-square approximation (Relative fast)	
	L_2, C_2, M		
	L_1, L_2, C_1, C_2		

parameter bounds used in the least square approximation are shown in Table XII.

Based on Tables IX–XI, as the number of unknowns increases, the estimation accuracy decreases. But if the difference between the actual value and the nominal value is severe, the estimation accuracy will also decrease. Therefore, one should find a balance between the accuracy and the number of unknowns to be estimated according to the actual setup. In addition, based on these three tables, the relative errors of L_1, C_1, and M are much larger than that of L_2, C_2, this is partly due to the sensitivity of L_1, C_1, and M to $|Z_{\text{in2\_}\omega}|$. If one wants to improve the estimation accuracy of L_1, C_1, and M, changing the estimation model from $|Z_{\text{in2\_}\omega}|$ to other models may work (for instance, model of Z_{in1}). While this article only focuses on receiver reactance identification, improving the accuracy of other parameters will not be discussed.

With the above analysis, the comparisons of this article and other papers are concluded in Table XIII, which is sorted from large maximum relative error to small error. It shows that the estimation accuracy of this proposal is at an average level. Notice that except for this article, the rest proposals in Table XIII are based on the transmitter-side, which may be unsuitable for later receiver-side reactance regulation because they need extra wireless communication to send the information of receiver reactance to receiver for tuning resonance.

IV. CONCLUSION AND FUTURE WORK

Obtaining the receiver reactance is one of the most crucial steps for tuning the receiver to resonant, so, this article proposes a PDM-based method to identify the inductor and capacitor of the receiver. Only the magnitudes of voltage and current into ASPR are needed for estimation. The parameter deviations of mutual inductance and transmitter-side parameters are also considered, the experimental results prove reasonably accurate estimation. Compared with previous receiver reactance identification methods, this proposal has two main contributions: 1) Neither wireless communication, synchronization with transmitter, nor extra hardware is needed; 2) implemented on the receiver-side, output stable power during the identification process.

It is worth mentioning that the calculation time in this experiment is 2–5 s. Compared with only 65 ms in the study [38], this computation time may be too long to apply fast monitoring. Since 2–5 s are negligible compared with the average charging time of the lithium battery (Model:18650) which is 4 h, this proposal is more suitable for stationary applications.

There are still some unsolved problems, for instance, the universal receiver. Mathematically, the fundamental principle of this identification method is using at least two model-based equations to calculate the two unknown parameters. But the model-based equations depend on the practical setup, which means the equations may be very complex and involve a quantity of system parameters for some WPT systems. Taking the multireceiver IPT system with cross-coupling in [39] as an example, based on (29) of [39], the receiver reactance is not only affected by the inductor and capacitor, but also by loads of other receivers. Thus, in the corresponding model-based equations, loads of other receivers should also be set as unknowns. As the number of unknown parameters and the complexity of the equation increase, the accuracy of the identified results is highly likely to decrease, and the computation time will increase. So, for the universal rectifier design, the accuracy of identification may be a point worth further study.

REFERENCES

[1] G. A. Covic and J. T. Boys, "Inductive power transfer," *Proc. IEEE*, vol. 101, no. 6, pp. 1276–1289, Jun. 2013.

[2] S. Q. Li and C. C. Mi, "Wireless power transfer for electric vehicle applications," *IEEE J. Emerg. Sel. Topics Power Electron.*, vol. 3, no. 1, pp. 4–17, Mar. 2015.

[3] H. H. Wu, A. Gilchrist, K. D. Sealy, and D. Bronson, "A high efficiency 5 kW inductive charger for EVs using dual side control," *IEEE Trans. Ind. Informat.*, vol. 8, no. 3, pp. 585–595, Aug. 2012.

[4] B. Teck Chuan, I. Takehiro, K. Masaki, and H. Yoichi, "Basic study of improving efficiency of wireless power transfer via magnetic resonance coupling based on impedance matching," in *Proc. IEEE Int. Symp. Ind. Electron.*, 2010, pp. 2011–2016.

[5] D. Kim and D. Ahn, "Self-tuning LCC inverter using PWM-controlled switched capacitor for inductive wireless power transfer," *IEEE Trans. Ind. Electron.*, vol. 66, no. 5, pp. 3983–3992, May 2019.

[6] N. A. Keeling, G. A. Covic, and J. T. Boys, "A unity-power-factor IPT pickup for high-power applications," *IEEE Trans. Ind. Electron.*, vol. 57, no. 2, pp. 744–751, Feb. 2010.

[7] Y. G. Su, H. Zhang, Z. Wang, A. Patrick Hu, L. Chen, and Y. Sun, "Steady-state load identification method of inductive power transfer system based on switching capacitors," *IEEE Trans. Power Electron.*, vol. 30, no. 11, pp. 6349–6355, Nov. 2015.

[8] C. Wang, C. Zhu, G. Wei, J. Zhang, and F. Liu, "Switched-capacitor tuning for three-phase wireless power receiver based on perturbation and observation method," *IEEE Access*, vol. 9, pp. 45189–45200, 2021.

[9] D. Ahn and S. Hong, "Effect of coupling between multiple transmitters or multiple receivers on wireless power transfer," *IEEE Trans. Ind. Electron.*, vol. 60, no. 7, pp. 2602–2613, Jul. 2013.

[10] T. C. Beh, M. Kato, T. Imura, S. Oh, and Y. Hori, "Automated impedance matching system for robust wireless power transfer via magnetic resonance coupling," *IEEE Trans. Ind. Electron.*, vol. 60, no. 9, pp. 3689–3698, Sep. 2013.

[11] R. K. Mai, Y. R. Liu, Y. Li, P. Yue, G. Cao, and Z. He, "An active-rectifier-based maximum efficiency tracking method using an additional measurement coil for wireless power transfer," *IEEE Trans. Power Electron.*, vol. 33, no. 1, pp. 716–728, Jan. 2018.

[12] R. Mai, P. Yue, Y. Liu, Y. Zhang, and Z. He, "A dynamic tuning method utilizing inductor paralleled with load for inductive power transfer," *IEEE Trans. Power Electron.*, vol. 33, no. 12, pp. 10924–10934, Dec. 2018.

[13] Y. Yang, S. Tan, and S. Y. R. Hui, "Front-end parameter monitoring method based on two-layer adaptive differential evolution for SS-compensated wireless power transfer systems," *IEEE Trans. Ind. Informat.*, vol. 15, no. 11, pp. 6101–6113, Nov. 2019.

[14] D. Y. Lin, J. Yin, and S. Y. R. Hui, "Parameter identification of wireless power transfer systems using input voltage and current," in *Proc. IEEE Energy Convers. Congr. Expo.*, 2014, pp. 832–836.

[15] A. Testa *et al.*, "Interharmonics: Theory and modeling," *IEEE Trans. Power Del.*, vol. 22, no. 4, pp. 2335–2348, Oct. 2007.

[16] G. B. Joung, C. T. Rim, and G. H. Cho, "An integral cycle mode control of series resonant converter," in *Proc. 19th Annu. IEEE Power Electron. Specialists Conf.*, Apr. 1988, pp. 575–582.

[17] H. Fujita and H. Akagi, "Pulse-density-modulated power control of a 4 kW, 450 kHz voltage-source inverter for induction melting applications," *IEEE Trans. Ind. Appl.*, vol. 32, no. 2, pp. 279–286, Mar./Apr. 1996.

[18] M. Y. Fan, L. M. Shi, Z. G. Yin, and Y. Li, "A novel pulse density modulation with semi-bridgeless active rectifier in inductive power transfer system for rail vehicle," *CES Trans. Elect. Mach. Syst.*, vol. 1, no. 4, pp. 397–404, Dec. 2017.

[19] M. Y. Fan, L. M. Shi, Z. G. Yin, L. Jiang, and F. Zhang, "Improved pulse density modulation for semi-bridgeless active rectifier in inductive power transfer system," *IEEE Trans. Power Electron.*, vol. 34, no. 6, pp. 5893–5902, Jun. 2019.

[20] H. C. Li, S. X. Chen, J. Y. Fang, Y. Tang, and M. A. de Rooij, "A low-subharmonic, full-range, and rapid pulse density modulation strategy for ZVS full-bridge converters," *IEEE Trans. Power Electron.*, vol. 34, no. 9, pp. 8871–8881, Sep. 2019.

[21] H. Li, J. Fang, S. Chen, K. Wang, and Y. Tang, "Pulse density modulation for maximum efficiency point tracking of wireless power transfer systems," *IEEE Trans. Power Electron.*, vol. 33, no. 6, pp. 5492–5501, Jun. 2018.

[22] Y. Chen *et al.*, "Reconfigurable topology for IPT system maintaining stable transmission power over large coupling variation," *IEEE Trans. Power Electron.*, vol. 35, no. 5, pp. 4915–4924, May 2020.

[23] X. H. Qu, H. Han, S. Wong, C. K. Tse, and W. Chen, "Hybrid IPT topologies with constant current or constant voltage output for battery charging applications," *IEEE Trans. Power Electron.*, vol. 30, no. 11, pp. 6329–6337, Nov. 2015.

[24] J. W. Liu, G. B. Wang, G. Xu, J. Peng, and H. Jiang, "A parameter identification approach with primary-side measurement for DC-DC wireless-power-transfer converters with different resonant tank topologies," *IEEE Trans. Transp. Electrific.*, vol. 7, no. 3, pp. 1219–1235, Sep. 2021.

[25] J. Yin, D. Y. Lin, C. K. Lee, T. Parisini, and S. Y. Hui, "Front-end monitoring of multiple loads in wireless power transfer systems without wireless communication systems," *IEEE Trans. Power Electron.*, vol. 31, no. 3, pp. 2510–2517, Mar. 2016.

[26] J. Nocedal and S. J. Wright, *Outline of the Trust-Region Approach in Numerical Optimization*. New York, NY, USA: Springer, 2006, Ch. 4, pp. 66–70.

[27] X. R. Sheng and L. M. Shi, "Mutual inductance and load identification method for inductively coupled power transfer system based on auxiliary inverter," *IEEE Trans. Veh. Technol.*, vol. 69, no. 2, pp. 1533–1541, Feb. 2020.

[28] R. M. Dai, W. Zhou, Y. Chen, Z. Zhu, and R. Mai, "Pulse density modulation based mutual inductance and load resistance identification method for wireless power transfer system," *IEEE Trans. Power Electron.*, to be published, doi: 10.1109/TPEL.2022.3153657.

[29] H. C. Li, K. Wang, J. Fang, and Y. Tang, "Pulse density modulated ZVS full-bridge converters for wireless power transfer systems," *IEEE Trans. Power Electron.*, vol. 34, no. 1, pp. 369–377, Jan. 2019.

[30] T. Mishima and C. M. Lai, "Load-adaptive resonant frequency-tuned -pulse density modulation for Class-D ZVS high-frequency inverter-based inductive wireless power transfer," *IEEE J. Emerg. Sel. Topics Ind. Electron.*, to be published, doi: 10.1109/JESTIE.2021.3102445.

[31] F. Zhou, "Online estimation algorithm for harmonic and interharmonic in power systems based on the quasi-synchronous sampling," (in Chinese), Ph.D. dissertation, Shanghai JiaoTong Univ., Shanghai, China, 2012, p. 73, Ch. 4.

[32] Y. M. Zhang, X. Li, S. Chen, and Y. Tang, "Soft switching for strongly coupled wireless power transfer system with 90° dual-side phase shift," *IEEE Trans. Ind. Electron.*, vol. 69, no. 1, pp. 282–292, Jan. 2022.

[33] X. R. Sheng and L. M. Shi, "An improved pulse density modulation strategy based on harmonics for ICPT system," *IEEE Trans. Power Electron.*, vol. 35, no. 7, pp. 6810–6819, Jul. 2020.

[34] M. K. Kazimierczuk and D. Czarkowski, "Class D current-driven rectifiers," in *Resonant Power Converters*, 2nd ed. Hoboken, NJ, USA: Wiley–IEEE Press, 2011 p. 31, Ch. 2.

[35] M. K. Kazimierczuk and D. Czarkowski, "Class D series-resonant inverters," in *Resonant Power Converters*, 2nd ed. Hoboken, NJ, USA: Wiley–IEEE Press, 2011, p. 184, Ch. 6.

[36] S. Hu, Z. Liang, Y. Wang, J. Zhou, and X. He, "Principle and application of the contactless load detection based on the amplitude decay rate in a transient process," *IEEE Trans. Power Electron.*, vol. 32, no. 11, pp. 8936–8944, Nov. 2017.

[37] Y. Su, L. Chen, X. Wu, A. P. Hu, C. Tang, and X. Dai, "Load and mutual inductance identification from the primary side of inductive power transfer system with parallel-tuned secondary power pickup," *IEEE Trans. Power Electron.*, vol. 33, no. 11, pp. 9952–9962, Nov. 2018.

[38] Y. Yang, S. C. Tan, and S. Y. R. Hui, "Fast hardware approach to determining mutual coupling of series–series-compensated wireless power transfer systems with active rectifiers," *IEEE Trans. Power Electron.*, vol. 35, no. 10, pp. 11026–11038, Oct. 2020.

[39] M. F. Fu, T. Zhang, X. Zhu, P. C. Luk, and C. Ma, "Compensation of cross coupling in multiple-receiver wireless power transfer systems," *IEEE Trans. Ind. Informat.*, vol. 12, no. 2, pp. 474–482, Apr. 2016.

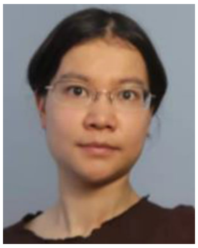

Ruimin Dai received the B.E. degree from Southwest Jiaotong University, Chengdu, China, in 2014, and the M.S. degree from Stony Brook University, Stony Brook, NY, USA, in 2015. She is currently working toward the Ph.D. degree from Southwest Jiaotong University, all in electrical engineering.

Her current research interests include wireless power transfer.

Ruikun Mai (Senior Member, IEEE) received the B.Sc. and Ph.D. degrees in electrical engineering from the School of Electrical Engineering, Southwest Jiaotong University, Chengdu, China, in 2004 and 2010, respectively.

He is currently a Professor with the School of Electrical Engineering, Southwest Jiaotong University, Chengdu, China. His research interests include wireless power transfer and its application in railway systems, power system stability, and control.

Wei Zhou (Member, IEEE) receive the B.E. and Ph.D. degrees from the School of Automation, Chongqing University, Chongqing, China, in 2013 and 2018, respectively, both in control theory and control engineering.

He was with the Department of Electrical, Computer and Software Engineering, The University of Auckland, Auckland, New Zealand from 2016 to 2017 as a visiting scholar. He is currently a Lecture with the School of Electrical Engineering, Southwest Jiaotong University, Chengdu, China. His current research interests include wireless power transfer technologies.